J. Fluid Mech. (2008), *vol.* 613, *pp.* 55–83.
doi:10.1017/S0022112008003091 Printed in the United Kingdom

Experimental study of physical mechanisms in the control of supersonic impinging jets using microjets

FARRUKH S. ALVI, HUADONG LOU, CHIANG SHIH AND RAJAN KUMAR

Department of Mechanical Engineering, Florida State University, 2525, Pottsdamer Street, Tallahassee, FL 32310, USA

(Received 13 September 2006 and in revised form 16 June 2008)

Supersonic impinging jet(s) inherently produce a highly unsteady flow field. The occurrence of such flows leads to many adverse effects for short take-off and vertical landing (STOVL) aircraft such as: a significant increase in the noise level, very high unsteady loads on nearby structures and an appreciable loss in lift during hover. In prior studies, we have demonstrated that arrays of microjets, appropriately placed near the nozzle exit, effectively disrupt the feedback loop inherent in impinging jet flows. In these studies, the effectiveness of the control was found to be strongly dependent on a number of geometric and flow parameters, such as the impingement plane distance, microjet orientation and jet operating conditions. In this paper, the effects of some of these parameters that appear to determine control efficiency are examined and some of the fundamental mechanisms behind this control approach are explored. Through comprehensive two- and three-component velocity (and vorticity) field measurements it has been clearly demonstrated that the activation of microjets leads to a local thickening of the jet shear layer, near the nozzle exit, making it more stable and less receptive to disturbances. Furthermore, microjets generate strong streamwise vorticity in the form of well-organized, counter-rotating vortex pairs. This increase in streamwise vorticity is concomitant with a reduction in the azimuthal vorticity of the primary jet. Based on these results and a simplified analysis of vorticity transport, it is suggested that the generation of these streamwise vortices is mainly a result of the redirection of the azimuthal vorticity by vorticity tilting and stretching mechanisms. The emergence of these longitudinal structures weakens the large-scale axisymmetric structures in the jet shear layer while introducing substantial three-dimensionality into the flow. Together, these factors lead to the attenuation of the feedback loop and a significant reduction of flow unsteadiness.

1. Introduction

It is well known that the impingement of a high-speed jet stream on a plane generally results in an unsteady flow field, which leads to a number of undesirable aeroacoustic-related effects. Significant among these are the substantially higher ambient noise levels in the jet vicinity, and very high unsteady pressure loads on the ground plane and nearby structures. Frequently, the noise and the unsteady pressure spectra are dominated by high-amplitude discrete tones commonly referred to as impingement tones, which can lead to a marked increase in sonic fatigue. From a practical perspective, this issue is of obvious interest as it is inherent in short take-off

and vertical landing (STOVL) aircraft, such as the Harrier or the STOVL version of the Joint Strike Fighter (JSF). From a fluid dynamics perspective this problem is of interest as it includes several canonical flow problems, such as viscous/inviscid interactions (especially in the impingement region), flow–acoustic coupling and flow–structure interactions, among others, making it a rich and challenging flow to study. This has led to a number of fundamental studies that examine the structure and fluid dynamic properties of this flow. Noteworthy among them are the classic investigations by Donaldson & Snedeker (1971*a*, *b*). Subsequently, Carling & Hunt (1974) and Kalghatgi & Hunt (1976), among others, have examined this flow, concentrating on the complex impingement region.

Studies on the aeroacoustics of impinging jets by Neuwerth (1974), Powell (1988), Tam & Ahuja (1990) and more recently by Krothapalli *et al.* (1999) have clearly established that the self-sustained, highly unsteady behaviour of the jet and the resulting impingment tones are governed by a feedback mechanism. The instability waves in the jet that originate at the nozzle exit grow (into large-scale structures) as they propagate downstream towards the impingement surface; acoustic waves are produced upon impingement of these structures which then travel upstream and excite the nascent shear layer near the nozzle exit. For further details on the feedback loop, see the articles cited above. Although the connection between the flow features of the impinging jet and the near-field hydrodynamic and noise field has been explored over a number of decades, more recently in studies by Alvi & Iyer (1999), Henderson (2002) and Henderson, Bridges & Wernet (2005), the details of this relationship are still not well-understood. However, what is well-accepted is the connection between the feedback loop and the related ground effect. Although the study of impinging jets has continued to be the focus of current research, the emphasis has more recently shifted to identifying control strategies to reduce the aforementioned adverse effects associated with this flow.

1.1. *Flow control approaches – a brief review*

The logical approach to control the adverse effects of impinging jet flow is to disrupt the feedback loop responsible for this unsteady behaviour. A number of strategies may potentially be used to accomplish this in order to control the unsteady properties of this flow. Some of the techniques, most of which are passive, include the use of: tabs (Samimy, Zaman & Reeder 1993), non-axisymmetric nozzle shapes (Zaman 1999), baffles (Elavarasan *et al.* 2000), co-flow (Sheplak & Spina 1994) and counter-flow (Shih, Alvi & Washington 1999).

Tabs have been shown to eliminate or reduce screech tones, whereas for some cases the mixing and shock-associated noise is reduced at lower frequencies but increases at higher frequencies. Using a nozzle with a design Mach number of 1.36, Samimy *et al.* (1993) reduced the OASPL (overall sound pressure level) of an underexpanded jet by about 6.5 dB using four tabs; however the reduction in noise was accompanied by a thrust penalty. Karamcheti *et al.* (1969) successfully suppressed edge tones in low-speed flows, which are governed by a similar feedback mechanism, by placing two plates normal to the jet centreline. Elavarasan *et al.* (2000) used a similar technique to attenuate the feedback loop in a supersonic impinging jet flow by introducing a control plate just outside the nozzle exit. This passive control method resulted in a reduction in the near-field OASPL by about 6–7 dB.

Sheplak & Spina (1994) used a high-speed co-flow to shield the main jet from the near-field acoustic disturbances. For a suitable ratio of the main jet and co-flow exit velocity, they measured a reduction of 10–15 dB in the near-field broadband

noise level in addition to the suppression of impinging tones. However, the very high mass flow needed for co-flow to achieve this makes this approach impractical. Shih *et al.* (1999) used counter-flow near the nozzle exit to successfully suppress screech tones of non-ideally expanded jets. They were also able to obtain modest reductions in OASPL, approximately 3–4 dB, while enhancing the mixing of the primary jet. A more detailed discussion of some of these control methods can be found in Alvi *et al.* (2003).

Although these techniques have shown varied promise, any significant performance gains were confined to a limited range of operating conditions, especially for impinging jets. This is due to the fact that a relatively small change in the nozzle-to-ground separation (h/d) can lead to a significant change in the magnitude and frequency of the tones that are responsible for the undesired flow unsteadiness. Therefore, there is a need for alternative methods, in particular those which do not interfere with the primary nozzle, and are also amenable to adaptive control.

In the present paper, we examine in some detail a flow control technique, which uses high-energy fluid streams to modify the jet shear layer and thus disrupts the azimuthally coherent interaction between the flow instabilities and the acoustic field. This approach was developed and explored by Alvi *et al.* (2003) and Lou, Alvi & Shih (2006) who describe earlier results of this ongoing study. Since the effects of microjet control have been discussed in these publications, they are only briefly described here to put the present results in perspective. The primary focus of this paper is to closely examine the flow field and its response to microjet control in order to gain a better understanding of the underlying mechanisms. The proposed control system has the advantage that, depending upon the operating flow conditions, optimal flow control can be achieved by activating the supersonic microjets at the appropriate conditions and they can be turned off when not needed. Therefore, the operational performance of the aircraft is not expected to be degraded when control is not needed. The very small size of the actuator hardware and the minimal mass flow rates require minimal power consumption. This, together with the fact that microjet control is applied downstream of the nozzle exit, should lead to minimal thrust loss of the primary jet. A more detailed description of the microjet control system hardware will be provided in the next section.

2. Experimental details

2.1. *Test configurations and facility*

The experiments were carried out at the STOVL supersonic jet facility of the Advanced Aero-Propulsion Laboratory (AAPL) located at the Florida State University. A schematic of the facility with a single impinging jet is shown in figure 1. The measurements were conducted using an axisymmetric, convergent-divergent (C–D) nozzle with a design Mach number of 1.5. The throat and exit diameters (d, d_e) of the nozzle are 2.54 cm and 2.75 cm, respectively (see figure 1). The divergent part of the nozzle is a straight-walled conic section with a 3° divergence angle from the throat to the nozzle exit. Although tests were conducted over a range of nozzle pressure ratios (NPR, where NPR = stagnation pressure/ambient pressure), the results discussed in the present paper are limited to NPR = 3.7 and 5.0. NPR = 3.7 corresponds to an ideally expanded Mach 1.5 jet, while NPR = 5 produces a moderately under-expanded jet. A circular plate of diameter D (25.4 cm $\sim 10d$) was flush mounted with the nozzle exit. This plate, henceforth referred to as the 'lift plate', represents a generic aircraft planform and has a central hole, equal to the nozzle exit diameter, through which

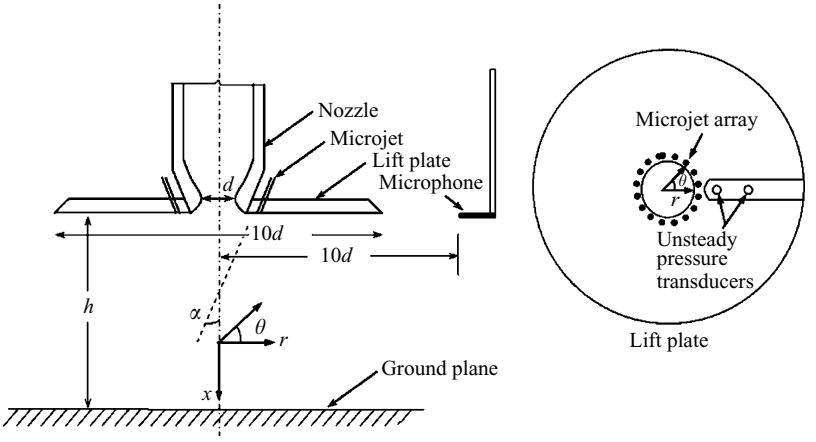

FIGURE 1. Schematic of the experimental arrangement.

the jet is issued (figure 1). A 1.0 m × 1.0 m aluminium plate serves as the ground plane and is mounted directly under the nozzle on a hydraulic lift. In order to obtain stereoscopic particle image velocimetry (PIV) measurements, the central portion of the ground plane was replaced by a glass plate for these experiments. Two CCD cameras were mounted under the ground plane, beneath this window (see figure 2), and were used to record the stereoscopic PIV images presented later in this paper. More details regarding the PIV arrangement are discussed in § 2.3.

Active flow control was implemented using microjets, flush mounted circumferentially around the main jet. The jets were fabricated using 400 μm diameter stainless tubes and were oriented at three different angles, 20°, 60° and 90°, with respect to the main jet axis. The air for the microjets was supplied from compressed nitrogen cylinders through a main and four secondary plenum chambers (see Alvi *et al.* 2003 for details). The microjets were operated over a range of NPR values (5–7), where the combined mass flow rate from all the microjets was less than 0.5% of the primary jet mass flux.

2.2. *Unsteady pressure and noise measurements*

The loads generated by the impinging jet flow were measured using high-frequency response miniature Kulite™ transducers installed on the lift plate and the ground plane. For the lift plate, three transducers (Model XCS-062, ±5 psid) were mounted at 35 mm, 45 mm and 58 mm, respectively, from the nozzle centreline (figure 1). Since the signals measured by all three lift plate transducers depict very similar trends, unless otherwise noted only data from the sensor closest to the nozzle are shown in this paper. The unsteady pressure field on the ground plane was measured with three high-frequency Kulite pressure transducers (Model XCQ-062, 100 psia); only representative data from the transducer located on the jet centreline are discussed herein. According to the manufacturer's specifications, these transducers have a flat frequency response up to 20% of their natural frequency, which corresponds to a minimum of 35 kHz for the lift plate and 65 kHz for the ground plane sensors, respectively. The use of these transducers for unsteady pressure measurements in low- and high-speed flows is well-established. The transducers signals were amplified, and low-pass filtered (35 kHz) using Stanford™ (Model SR640) filter/amplifiers. Using this signal-conditioning hardware, the noise floor for these transducers was generally 60 dB or more below the measured dynamic pressures. In addition to the pressure

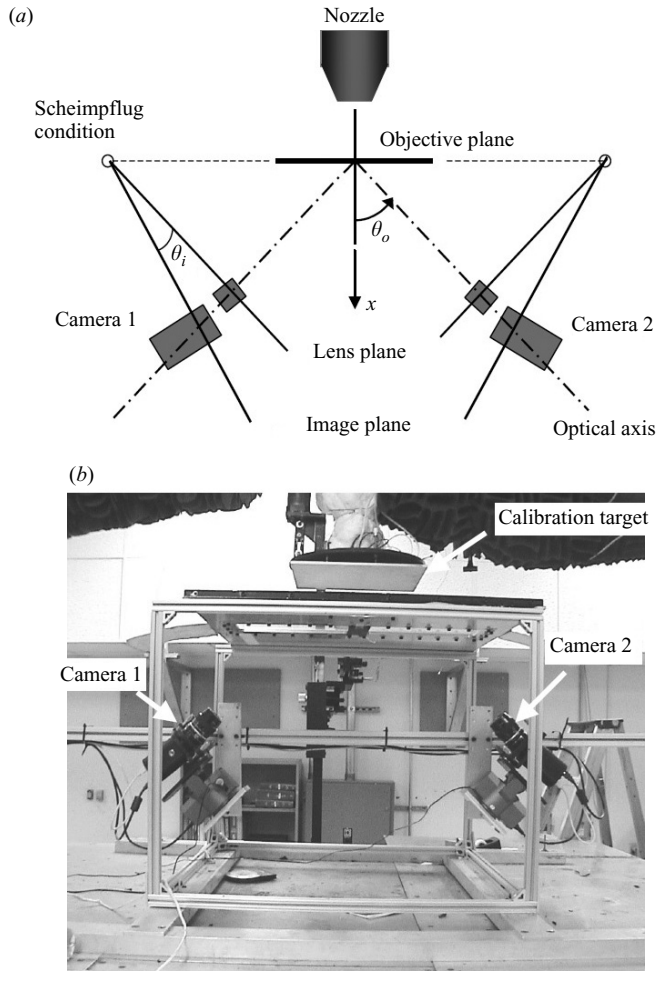

FIGURE 2. Experimental arrangement of the three-dimensional PIV system. (*a*) Scheimp flug condition; (*b*) experimental setup.

sensors, near-field noise was measured using a $\frac{1}{4}$ inch diameter B&K^{TM} microphone placed approximately 26.7 cm (10.5*d*) away from the nozzle centreline, oriented 90° to the jet axis (see figure 1). Sound reflections were minimized for the near-field acoustic measurements by covering exposed metal surfaces with 10 cm thick acoustic foam.

The microphone and the unsteady pressure signals were acquired through high-speed National Instruments digital data acquisition cards using the LabView^{TM} software. For unsteady measurements 100k points were recorded from each transducer and standard statistical analysis techniques were used to estimate the spectral content and the OASPL. The spectral content was obtained by segmenting each data record into 100 subgroups with 1k points each and a fast fourier transform (FFT) with a frequency resolution of 68.4 Hz was computed for each segment. The 100 FFTs thus obtained were averaged to obtain an estimate of the narrow-band noise spectra. The estimated uncertainty associated with the unsteady lift plate pressure, P_{rms}, is ± 0.02 psi while the r.m.s. intensities of the ground plane pressures were estimated to be accurate within ± 0.2 psi. The microphone signal was measured with an estimated uncertainty of ± 1 dB.

2.3. *Particle image velocimetry*

Non-intrusive PIV measurements, were used to obtain whole-field velocity data. The velocities were first measured in the streamwise central plane of the jet using a planar or two-dimensional PIV system. For selected cases, stereoscopic PIV was used to obtain the three-dimensional velocity field data at selected planes perpendicular to the jet centreline. For the sake of brevity, only a schematic of the experimental arrangement for the cross-plane PIV system is shown in figure 2.

In PIV measurements, the primary jet was seeded with small ($\sim$0.3 μm) oil droplets generated using a modified Wright Nebulizer. The ambient air was also seeded with smoke particles ($\sim$1–5 μm) produced by a Rosco-1600 fog generator. A double-pulsed Nd:YAG laser (Spectra-Physics, 400 mJ) was used for flow-field illumination. A laser light sheet, about 1 mm thick, was created using a combination of spherical and cylindrical lenses. The stereoscopic PIV setup used two SharpVison^{TM} Model 1400DE cameras consisting of Progressive Scan Interline CCD sensors (SONY ICX 085AL) to capture the images. Each camera has a resolution of 1280 (H) $\times$ 1024 (V) active pixels of size 6.7 μm $\times$ 6.7 μm. The planar images for the two-component velocity measurements were recorded using a cross-correlation CCD camera (Kodak ES 1.0) with 1k $\times$ 1k resolution. The images for both arrangements were acquired at a rate of 15 image pairs per second. The time delay between two laser pulses was optimized at $1 \sim 1.5$ μs depending on the jet operating condition. An image matching approach was used for the digital processing of the image pairs in order to calculate the displacement field. To obtain velocity data with a high spatial resolution, a novel processing scheme was used, details of which are described in Lourenco & Krothapalli (1998). We simply note that a principal advantage of this approach is that the velocity field is obtained with second-order accuracy; hence the spatial derivatives are computed with higher precision.

As stated earlier, the ground plane height h with respect to the nozzle exit can be varied from $2d$ to $60d$. However, the PIV results for only $h/d = 4$, are shown here, and the laser sheet position, x (see the coordinate frame in figures 1 and 2) with respect to the nozzle exit, was varied from $1d$ to $3d$. Experiments were conducted at NPR = 2.5, 3.7 and 5, which correspond to an over-expanded, ideally expanded and under-expanded primary jet flow, respectively. However, PIV results presented here will be limited to NPR = 3.7 and 5. The jet was mildly heated to avoid condensation of the ambient air entrained into the jet during the PIV measurements. The jet stagnation temperature was nominally maintained at 320 ± 5 K. Although not shown here, the flow was also visualized using a single-pass shadowgraph arrangement (Lou *et al.* 2006).

3. Results and discussion

Previous studies (Alvi *et al.* 2003; Lou *et al.* 2006) clearly demonstrated that the use of microjets dramatically reduces both the impinging tones and the overall noise levels for supersonic impinging jets. To provide a context for the main results discussed in this paper, a very brief summary of some of the results of our earlier work is provided here. See the above articles for a detailed discussion. As discussed in Alvi *et al.* (2003), shadowgraph images of the uncontrolled impinging jet (not shown here) clearly show the presence of large, axisymmetric, structures in the jet shear layer as well as the presence of visible acoustic waves in the ambient environment. Collectively, these provide visual evidence of the strong feedback loop responsible for the highly unsteady flow (also see Krothapalli *et al.* 1999). The activation of microjets nearly

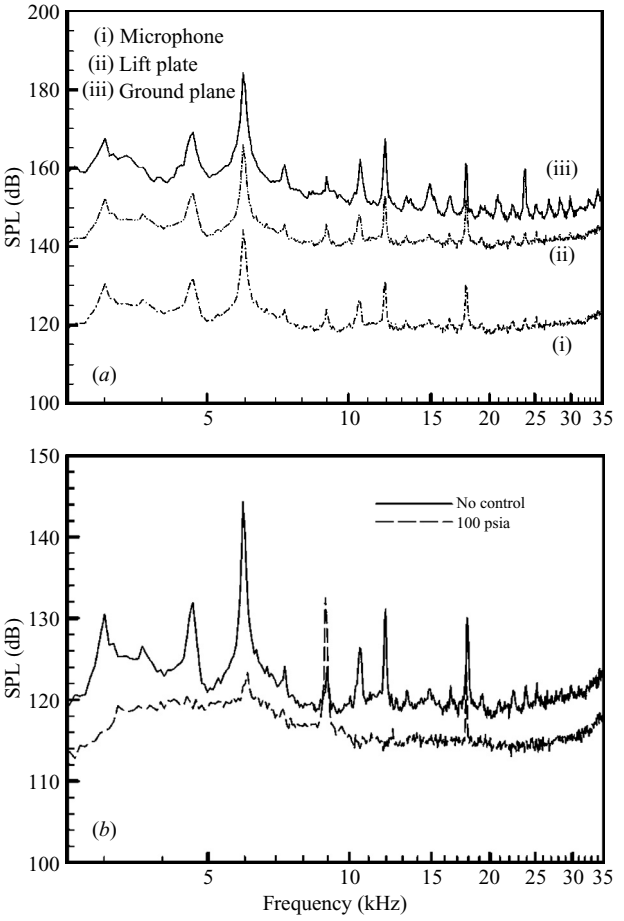

FIGURE 3. Unsteady pressure spectra, $h/d = 4$. NPR = 3.7; (*a*) no control, Kulite and microphone signals; (*b*) microphone, with and without control.

eliminates the large-scale structures and the acoustic waves, suggesting a significant attenuation of resonance. These shadowgraphs also reveal 'streaks' generated by the supersonic microjets, which have been taken as an indicator of the presence of streamwise vorticity (Samimy *et al.* 1993; Krothapalli *et al.* 1999). Based on these visualizations we have speculated that the production of streamwise vorticity may in part be responsible for the reduction in the flow unsteadiness. In § 3.2, we provide more direct evidence to support this hypothesis.

In figure 3(*a*), we show the narrow-band, unsteady pressure spectra measured at all three transducer locations: lift plate, ground plane, and the near-field microphone. As seen here, large-amplitude, narrow-band peaks are seen at all three locations, indicating the presence of impingement tones due to flow–acoustic coupling. The fact that the frequencies of these tones are nearly identical at all three locations further confirms the global nature of this resonance. In figure 3(*b*), we show representative results depicting the effect of microjet control on the near-field noise for NPR 3.7, $h/d = 4$. Although a range of microjet pressures were tested, the data shown here correspond to the microjets operating at 100 psia. (The effect of microjet pressure on control efficiency will be briefly discussed later.) A comparison of the two spectra

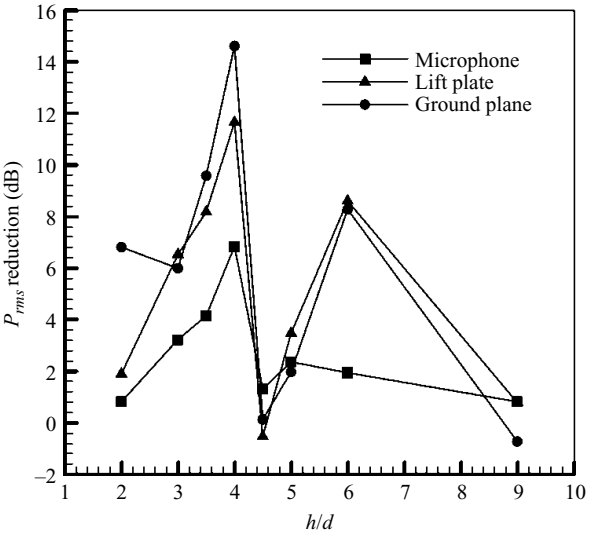

FIGURE 4. Reductions in fluctuating pressure intensities as a function of h/d, NPR = 3.7 (20° microjets at 100 psi).

in figure 3(*b*), reveals that the distinct tones in the uncontrolled impinging jet are significantly diminished by the activation of microjets. Equally noteworthy is the fact that tonal attenuation is accompanied by a broad-band reduction in the spectral amplitudes.

The effect of microjet control on the lift plate and ground plane unsteady pressures is very similar to that seen in figure 3(*b*). However, the actual magnitude of reduction varies with sensor location as well as with the main jet operating conditions. Figure 4 summarizes the overall reductions due to microjet control, measured at all three locations, for an ideally expanded jet (NPR = 3.7). This plot clearly shows that the fluctuating loads are significantly reduced at almost all of the heights examined. Similar, but larger, reductions were seen for under-expanded jets (see Alvi *et al.* 2003 and Lou *et al.* 2006).

As seen in figure 4, at a given NPR, the magnitude of reduction is strongly dependent upon the ground plane distance (h/d). In an attempt to understand this dramatic change in control efficacy with impingement plane distance, in figure 5 we show the pressure spectra at $h/d = 4$ (where the microjets are most effective) and at $h/d = 4.5$ (microjets are minimally effective) for the ideally expanded jet without control. A careful comparison of the unsteady pressure spectra at the two heights reveals that the frequency spectrum at $h/d = 4.5$ (figure 5*b*) is dominated by a single, high-amplitude impingement tone. The amplitude of this dominant tone is about 20 dB higher than the secondary tones. This suggests that the feedback loop at this height (and NPR) is very strongly 'locked' on this single frequency and hence much higher energy input may be required in order to eliminate this robust impingement tone. In contrast, multiple impinging tones appear in the spectrum of $h/d = 4$ in figure 5(*a*), where these tones are out of phase (Lou 2005). It is possible that the competition between different modes at $h/d = 4$ leads to a less robust feedback loop for a particular frequency/phase value, making it more amenable to disruption due to the microjets. The presence of multiple modes which often interact with each other is a phenomenon often observed in flows governed by a feedback process, such

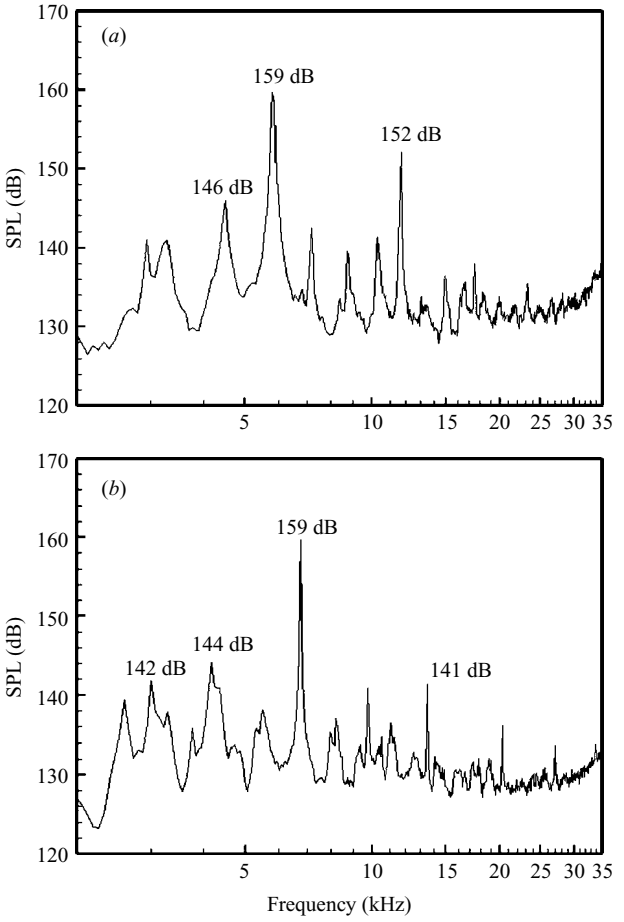

FIGURE 5. Unsteady pressure spectra, NPR = 3.7. (*a*) $h/d = 4.0$; (*b*) $h/d = 4.5$.

as flows over cavities. Although a number of studies have attempted to examine this interaction – for example, see Kegerise *et al.* (2004), this behaviour is still not well-understood and this issue is far from resolved.

Finally, the efficiency of reduction also appears to have a 'staging' behaviour as seen in figure 4. This trend of non-uniform reductions for the microjet control might be also related to the well-known staging behaviour of the impingement tones with ground plane distance, as discussed in some detail in Krothapalli *et al.* (1999). The non-uniform reductions suggest that efficient control of this flow requires an adaptive control approach where the microjets need to be adaptively manipulated to provide optimal control at all heights.

3.1. *Microjet parameters and their effect on unsteady pressures and noise*

In order to examine the effect of microjet control parameters and configuration on the overall flow control efficacy, and to provide some insight into the physical mechanisms behind this control scheme, a comprehensive parametric study was conducted. The parameters varied include: microjet angle, microjet operating pressure, number/spacing of microjets, the use of microtabs instead of microjets, microjet size and spatial distribution of microjets relative to the main jet. A comprehensive discussion of the influence of these parameters can be found in Lou *et al.* (2006). For

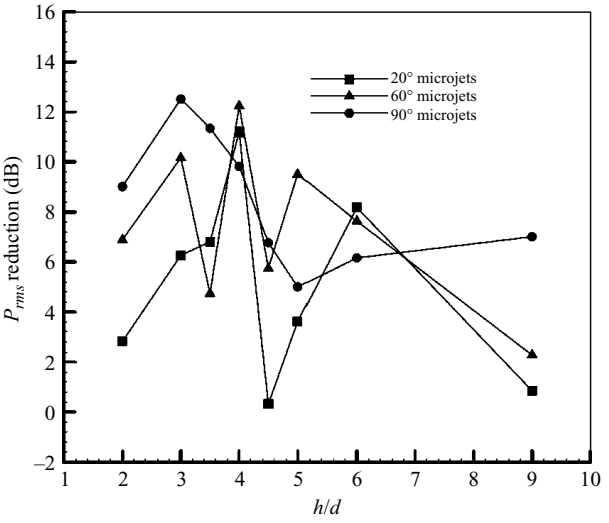

FIGURE 6. Effect of microjet angle on the reductions of fluctuating pressure intensities; NPR = 3.7.

the sake of brevity, only the effects of microjet angle, pressure and spacing on control efficiency are briefly discussed here.

3.1.1. *Microjet angle*

Our early studies (Alvi *et al.* 2003) revealed that 20° microjets are more effective for the under-expanded jets than for ideally and over-expanded cases. It was postulated that this difference was due to the curvature of the jet boundary when the jet is under-expanded, making it easier for the microjet streams to penetrate into the shear layer of the primary jet. If this is indeed the case, deeper penetration of the control jets can also be achieved by varying the microjet angle without increasing the control effort (microjet pressure). As discussed next, this was explored by testing three different microjet injection angles.

For the ideally expanded case shown in figure 6, the reduction in unsteady loads on the lift plate increases for almost all heights when the angle is changed from 20° to 60° or 90° (microjet operating pressure is fixed at 100 psia). This increase in the control efficacy is quite substantial as the P_{rms} levels on the lift plate and ground plane (not shown) are attenuated by an additional 5 to 8 dB relative to the 20° microjets. The change is even more dramatic at certain heights, such as $h/d = 2.0, 4.5, 9.0$, where the 20° microjet control is least effective. The fact that the 90° microjets cannot 'intercept' the acoustic waves but still manage to provide more effective control than 20° microjets implies that the acoustic 'shielding' of the primary jet shear layer from the ambient acoustic wave by the microjet streams is probably not the main mechanism behind this control scheme. This does not preclude the possibility that shielding may play a secondary role for other microjet configurations (in terms of injection angle).

It should be noted that the interaction point between microjet streams and the primary jet shear layer is different when different microjets angles are used (see figure 1). For example, 90° microjet streams penetrate into the primary jet shear layer at the nozzle exit. However, the interaction point between the 20° microjet stream and the primary jet shear layer occurs further downstream. This will probably influence

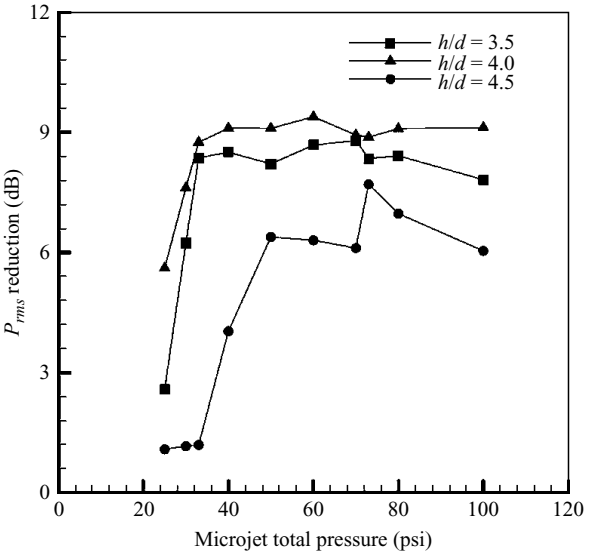

FIGURE 7. Effect of microjet pressure on the reductions of fluctuating pressure intensities on the lift plate; NPR = 3.7, 60° microjets.

the efficacy of microjet control since the jet shear layer is most receptive to external inputs at the nozzle exit. Unfortunately, due to limitations in the test geometry, we were unable to independently fix this parameter while exploring the influence of others. However, using similar microjet actuators, jet noise control experiments have been conducted by Greska (2005) where the interaction point between the microjet stream and the primary shear layer was fixed while the microjet angle was varied. His results indicated that maximum noise reduction was achieved when a 70° injection was used, suggesting that injection angle is a governing parameter independent of injection location. In § 3.3, this issue will be further explored in the context of the velocity field data.

3.1.2. *Microjet pressure*

The penetration depth of the microjet stream into the primary jet shear layer is another parameter expected to influence the efficacy of microjet control. Papamoschou & Hubbard (1993) among others have demonstrated that the penetration depth of a jet in a crossflow is strongly dependent on the momentum ratio of the control jet flow relative to the main (jet) flow. In the present study, for a given primary jet operating condition, the momentum ratio is only a function of the microjet stagnation pressure. Therefore, microjet penetration depth can be directly related to the microjet operating pressure.

Figure 7 shows reductions of the unsteady pressure loads as a function of microjet pressure, for an ideally expanded jet, using 60° microjets. As seen here for $h/d = 3.5$ and 4.0, substantial reductions are observed even at very low microjet pressures. Initially, the P_{rms} reductions increase rapidly as the microjet pressure is increased between from 25 psia to 35 psia. This is followed by saturation in performance, occurring around 40 psia for this configuration, where further increments in the microjet pressure show minimal, if any, additional gains. This reinforces the intuitive notion that penetration depth is an important parameter in developing an efficient control scheme and that the microjet streams influence the flow most effectively

through direct interaction with the primary jet shear layer. However, once the microjet streams have fully penetrated the primary jet shear layer, stronger microjets may not provide additional control. In contrast to $h/d = 3.5$ and 4, very little reduction is achieved at low microjet pressures (<35 psia) for $h/d = 4.5$, a height where microjet control has been the least effective. As the penetration depth into the primary jet should be comparable for all operating heights, one would expect control to be equally effective at these low operating pressures for $h/d = 4.5$ also, *if* the penetration depth is the only primary factor. Instead, control efficiency becomes measurable at higher pressures (>35 psia) and similarly saturates at a much higher pressure (>60 psia), relative to $h/d = 3.5$ and 4. As noted in the discussion of figure 5, since the feedback process is apparently much stronger for $h/d = 4.5$, it follows that the minimal pressure required to disrupt the resonance is higher; however this is an area that needs to be explored further.

3.1.3. *Microjet spacing*

The spacing between the microjets, i.e. the distance between the perturbations induced by the microjets, is also a variable that may be of some importance. Although at present very limited data are available for jet flows, extensive experimental (Meiburg & Lasheras 1988; Lasheras & Meiburg 1990; Julien, Lasheras & Chomaz 2003), and theoretical (Widnall, Bliss & Tsai 1974; Pierrehumbert & Widnall 1982) studies on the planar mixing layer have shed some light on this topic. In these studies, possible physical mechanisms responsible for the emergence of three-dimensional instability in parallel shear flows have been proposed. Based on their study of the plane mixing layer, Pierrehumbert & Widnall (1982) discovered a relationship between the wavelengths of the primary and secondary instabilities. They also note that the primary vortex is pushed into the free stream, where a significant streamwise vorticity component is generated through a stretching and tilting of the primary vortex. This streamwise vorticity takes the form of pairs of counter-rotating streamwise vortices (see figure 9 in Pierrehumbert & Widnall 1982). Subsequent studies by Meiburg & Lasheras (1988), Lasheras & Meiburg (1990) and Julien *et al.* (2003) confirmed their findings that the wavelength of the three-dimensional mode, λ_{D3}, is strongly related to the wavelength of the primary, two-dimensional instability, λ_{D2}.

Guided by some of the work cited above, limited experiments were conducted, exploring the existence of an optimal range of inter-microjet spacing that may make this control technique more efficient by exploiting the generation of secondary instabilities and streamwise vorticity. This was accomplished using three different configurations of 8, 16, and 32 microjets, circumferentially distributed around the nozzle with equal spacing. The details of these experiments can be found in Lou *et al.* (2006). Suffice it to say that, using this rather limited parametric range (only three microjet spacing configurations), the results show that 16 microjets provided the best effectiveness. A reduction in spacing beyond this value, i.e. using more than 16 microjets while keeping other parameters constant, actually reduced control efficacy. More studies over a larger parametric space are needed; however with this caveat in mind, these results do suggest the existence of a preferred spacing that may be related to the wavelength of secondary instabilities.

3.2. *The velocity and vorticity field*

In order to facilitate the discussion of the velocity and vorticity fields, we first define the most important velocity and vorticity variables used in subsequent sections. The subscripts x, r, θ refer to the axial, radial and azimuthal components,

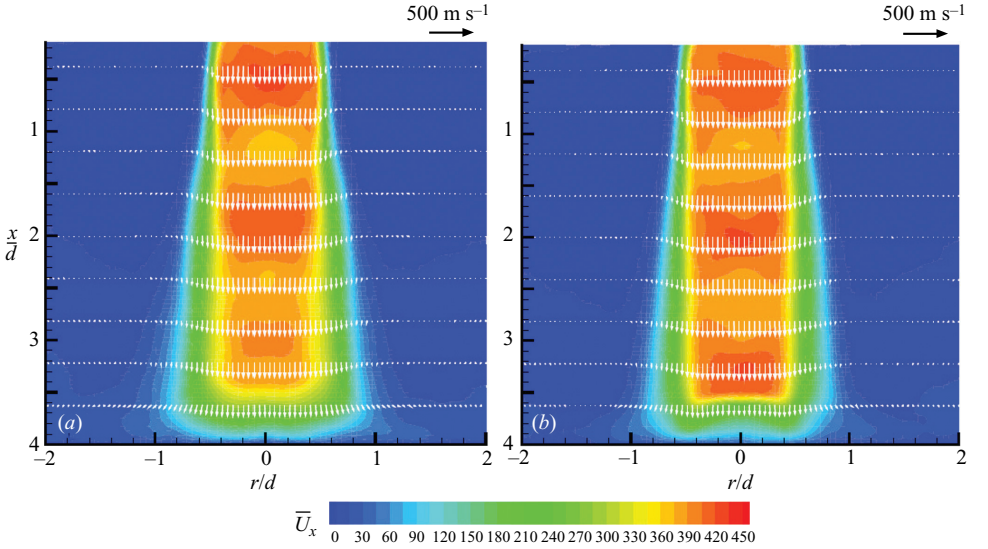

FIGURE 8. Ensemble-averaged streamwise velocity distribution in the centreplane of the jet flow. NPR = 3.7, $h/d = 4$. (*a*) No control; (*b*) with control.

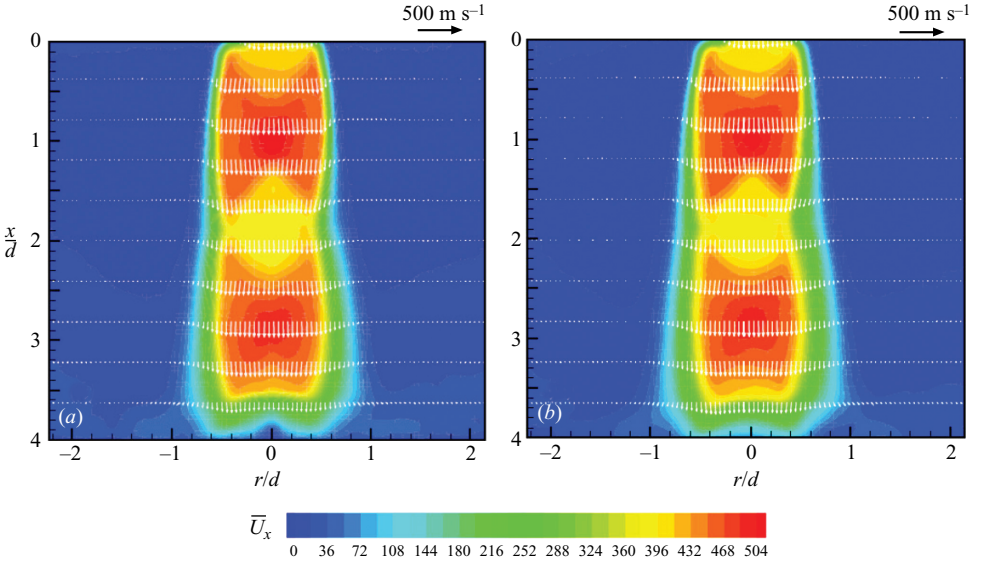

FIGURE 9. As figure 8 but for NPR = 5.

respectively, in the cylindrical coordinate system. This is shown in figure 1 with respect to the test configuration. The variables of interest are defined as follows:

U_x: streamwise velocity
U_r: radial velocity
U_θ: azimuthal velocity
$\overline{U_x}$: mean streamwise velocity
Ω_x: streamwise vorticity
Ω_r: radial vorticity
Ω_θ: azimuthal vorticity
U_j: U_x at the nozzle exit

3.2.1. *Shear layer of the primary jet*

In order to gain a better understanding of the effect of microjets on the flow field, planar PIV measurements were carried out along the streamwise central plane of the jet. Contour plots of the mean velocity distribution for NPR 3.7 and 5 are shown in figures 8 and 9, respectively, where velocity vector profiles are superimposed at selected streamwise locations. These plots are obtained by averaging data from 400 instantaneous PIV whole-field measurements, thus providing a reliable estimate of the mean velocity field. In principle, Mach 1.5 should be shock-free at NPR = 3.7, which corresponds to the ideally expanded condition. However, a weak periodic shock-cell structure can be seen in the velocity contour plots in figure 8(*a*). This is because the finite lip thickness of the nozzle exit will always generate shock waves, albeit weak ones. Furthermore, the entrainment of the ambient air into the jet, which is significant for an impinging jet flow field (Krothapalli *et al.* 1999; Alvi *et al.* 2003), generates a low pressure on the lift plate and in the vicinity of the nozzle exit. This results in a very weakly under-expanded jet at the nozzle exit.

For a moderately under-expanded jet operating at NPR = 5, the shock-cell structure is stronger and more clearly evident in figure 9. The shock-cell spacing can be easily measured from the identifiable peaks and valleys in the velocity distribution along the centreline of the jet. The measured shock-cell spacing, about 1.8*d*, at this Mach number agrees fairly well with Tam's correlation (Tam 1988). Interestingly, upon comparing figures 8(*a*) and 9(*a*), the baseline flow, to figures 8(*b*) and 9(*b*), the corresponding control cases, at first there appears to be no dramatic differences in the global features of the jet velocity fields, at least qualitatively (as subsequently discussed, there are significant differences in many details). This is interesting given the fact that the unsteady flow behaviour has been drastically modified, as demonstrated by the changes in the unsteady pressures and noise due to microjet control. The relatively small impact on the global mean velocity suggests that primary jet properties in terms of thrust are not substantially altered by the microjet control, an important consideration for a scheme if it is to be implemented in a practical system. However, direct thrust measurements are needed to confirm this. Furthermore, whether even small thrust losses are acceptable will have to be examined in the context of specific applications.

Considering the fact that the initial shear layer growth has a profound effect on the overall instability, we next examine the influence of microjet control on the shear layer characteristics. To quantify the growth of the shear layer, the shear layer width, δ, is defined as $\delta = r_{0.1} - r_{0.9}$; here $r_{0.1}$and $r_{0.9}$ are the radial locations where the local mean velocities reach 10% and 90% of the local jet centreline velocity, respectively. Based on this definition, the evolution of the shear layer as a function of the streamwise distance from the nozzle, x/d, is presented in figure 10; for both the baseline and the microjet-controlled case. Two observations can be made here: First, the shear layer with microjet control (filled symbols) is initially thicker – roughly for $x/d < 1$ when compared to the no-control case. As discussed in § 3.2.2 (ii) and illustrated in figure 18, the local thickening of the jet shear layer near the nozzle exit can be directly related to the emergence of strong streamwise vortices due to the microjets. This increase of the shear layer thickness in the initial region can in turn reduce the receptivity of the shear layer and therefore limit the number of unstable modes (Bradshaw 1987) supported by this shear layer. This leads to the second observation regarding the mean flow field: although the initial thickness is larger near the nozzle exit, further downstream the shear layer grows more slowly when control is activated. This is also visually evident upon comparing figures 8(*a*) and 9(*a*) to their respective control

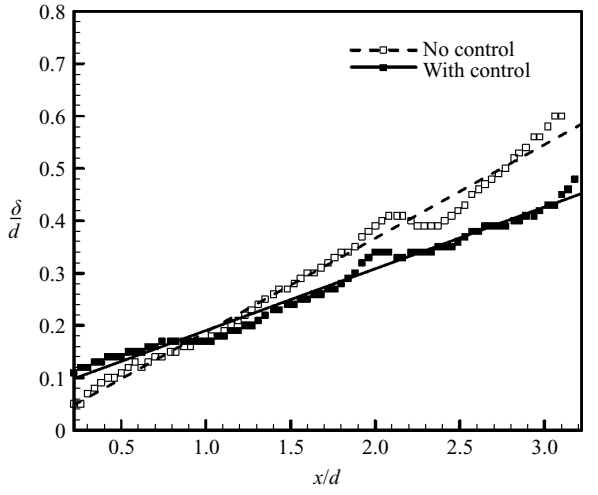

FIGURE 10. Streamwise variation of shear layer thickness; NPR = 3.7, $h/d = 4$, 90° microjet at 100 psia.

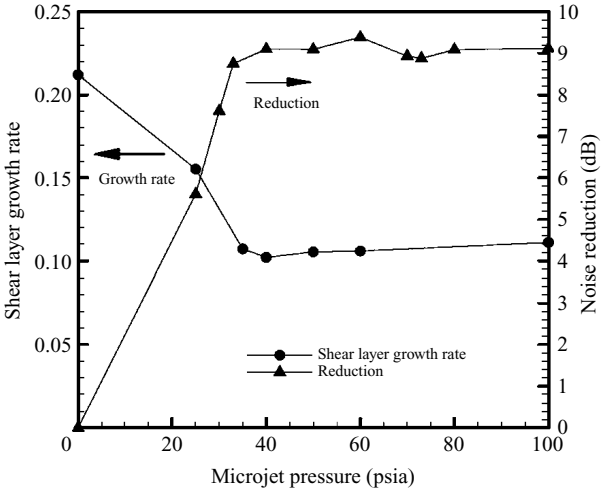

FIGURE 11. Effect of microjet operating pressure on shear layer growth rate; NPR = 3.7, $h/d = 4$, 60° microjets.

cases. This behaviour is consistent with the fact that the suppression of the feedback loop by microjets significantly stabilizes the overall flow unsteadiness, reducing the large-scale shear layer structures and leading to a more subdued flow development (Alvi *et al.* 2003).

Recalling that the results shown in figure 7 demonstrate that the reduction of flow unsteadiness is a function of microjet operating pressures, it is useful to also examine the shear layer growth with microjet pressure. This is explored in figure 11, which clearly illustrates that the variation of the shear layer growth rate ($d\delta/dx$) is inversely related to the microjet pressure. In addition, both trends asymptote toward constant values beyond the control saturation pressure (>40 psia) for this configuration. To summarize, the flow-field results discussed so far clearly suggest that the reduction in flow unsteadiness by microjets is in part due to the thickening of the intial shear layer

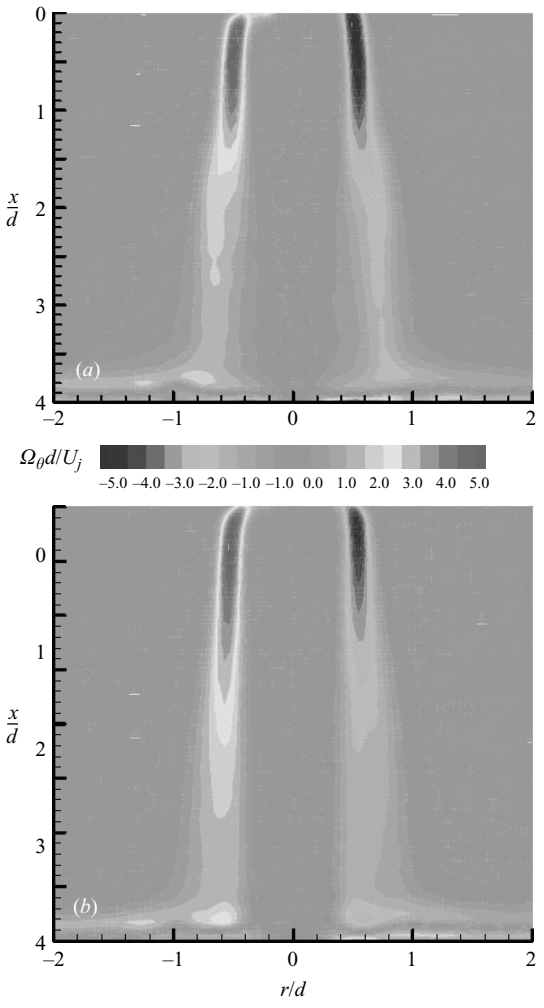

FIGURE 12. Ensemble-averaged vorticity distribution in the centreplane of the jet flow; NPR = 3.7, $h/d = 4$. (*a*) No control; (*b*) with control.

($x/d < 1$) of the primary jet which in turn makes it more stable and less susceptible to perturbations due to the feedback loop. The lower receptivity due to local shear layer thickening leads to a lower *global* growth of the jet downstream of $x/d = 1.0$.

3.2.2. *The vorticity field and its response to microjets*

(i) *The azimuthal vorticity field*

Flow visualization results of earlier studies (Alvi *et al.* 2003; Lou *et al.* 2006) clearly demonstrate that microjet control disrupts the feedback loop leading to the suppression of large-scale vortical structures, typically observed in uncontrolled impinging jets. In addition, the streamwise streaks visible in these shadowgraphs suggest the generation of streamwise vorticity due to microjets. Consequently, a closer examination of the vorticity field was conducted to further explore the fundamental mechanisms behind this control scheme.

Figures 12 and 13 show ensemble-averaged vorticity contour plots measured along the jet central plane for NPR of 3.7 and 5.0, respectively, where the contours show

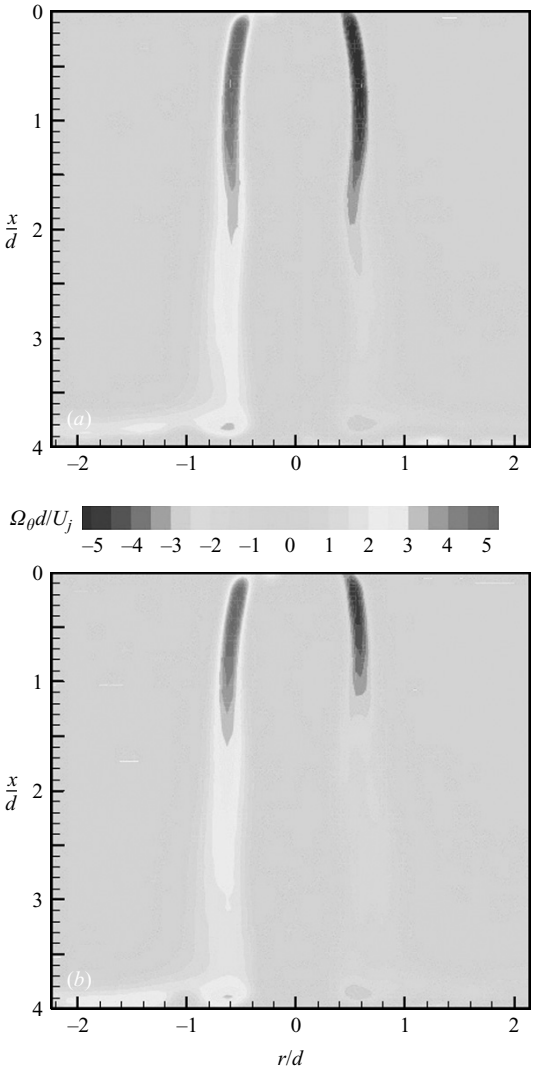

FIGURE 13. As figure 12 but for NPR = 5.

the azimuthal (out-of-plane) component of the normalized vorticity, $\Omega_\theta d/U_j$ (refer to figure 1 for the coordinate frame). Compared to the no-control cases (figures 12*a* and 13*a*), the azimuthal vorticity appears to be weaker when microjets are turned on, as seen in figure 12(*b*), and especially in figure 13(*b*). Although the contour plots show the global response of the vorticity field, the coarseness of the contour levels requires a closer look at the vorticity magnitudes. In figure 14, we show the azimuthal vorticity profiles extracted from these contour plots, where figures 14(*a*) and 14(*b*) correspond to NPR = 3.7 and figures 14(*c*) and 14(*d*) to NPR = 5. For each NPR, profiles at two downstream locations are shown where the filled symbols correspond to the microjet control case; data are only shown for half of the jet column. As seen in all four plots, microjets reduce the peak azimuthal vorticity in all cases, whereas the reduction is more substantial for the under-expanded case in figures 14(*c*) and 14(*d*). This is consistent with the shear layer growth results discussed earlier. As a first-order

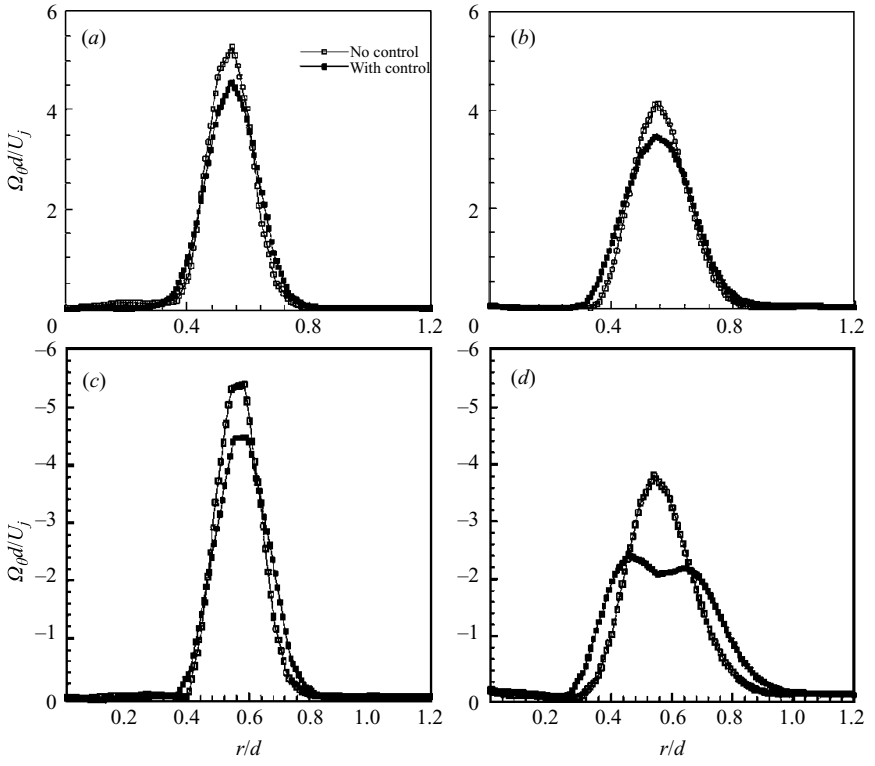

FIGURE 14. Radial variation of peak normalized vorticity. (*a*) NPR = 3.7, $x/d = 0.5$; (*b*) NPR = 3.7, $x/d = 1.0$; (*c*) NPR = 5.0, $x/d = 0.5$; (*d*) NPR = 5.0, $x/d = 1.5$.

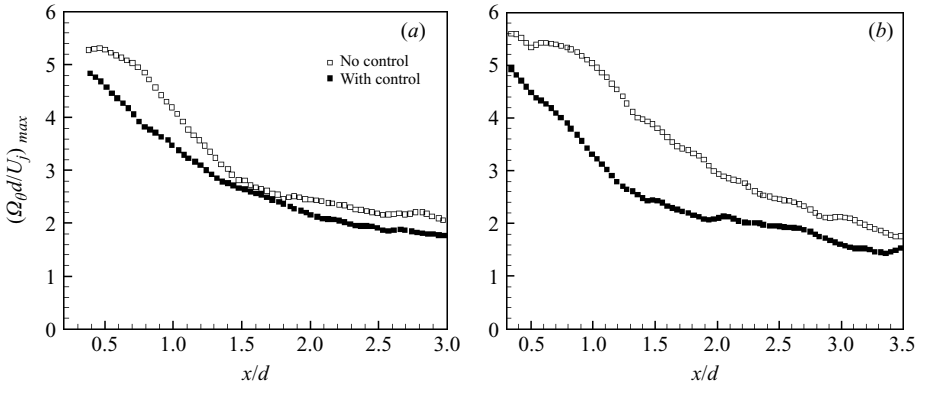

FIGURE 15. Axial variation of peak normalized vorticity. (*a*) NPR = 3.7, $h/d = 4$; (*b*) NPR = 5, $h/d = 4$.

approximation, near the nozzle exit the azimuthal vorticity can be approximated as: $\Omega_\theta \sim U_j/\delta$. Since, as shown in figure 10, the shear layer with microjet control is thicker near the nozzle exit, assuming U_j as roughly constant, the azimuthal vorticity should decrease in this region. This is confirmed by the vorticity measurements shown in figure 14.

To further investigate the streamwise evolution of azimuthal vorticity, the peak value of the locally normalized azimuthal vorticity, $(\Omega_\theta d/U_j)_{max}$ is shown as a function of x/d in figure 15. As expected, for all cases considered – baseline and with

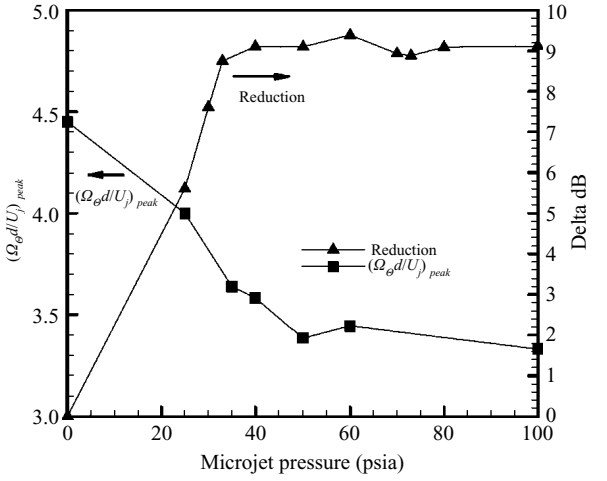

FIGURE 16. Effect of microjet operating pressure on the strength of azimuthal vorticity; NPR = 3.7, $h/d = 4$, 60° microjet.

control – the peak values decrease gradually as the jet expands downstream. More significantly, the peak values are lower with control for both ideally and under-expanded cases, where the difference between the two decreases downstream from the nozzle exit. The reduction of peak vorticity is much greater for the under-expanded case, consistent with the unsteady pressure measurements reported earlier. As an example, the azimuthal vorticity due to microjet control is reduced by as much as 40% for the under-expanded condition. The lower peak vorticity with control suggests a weakening of the azimuthal vortical structures, a result consistent with the disappearance of large-scale structures in the flow visualizations. The impact of these weakened structures on the ground leads to weaker upstream – propagating acoustic waves, resulting in a diminished forcing of the shear layer at the nozzle exit, which is already less receptive due to its increased thickness. This sequence of events leads to a significant weakening of the feedback loop and a subsequent reduction in the overall unsteadiness of the supersonic impinging jet flow.

Similar to figure 11, it is useful to examine the strength of azimuthal vorticity as a function of microjet operating pressure. Figure 16 shows the variation of the peak azimuthal vorticity measured at $x/d = 1.0$, and the reduction in the unsteady pressures (in Delta dB), as a function of the microjet pressure. Clearly, azimuthal vorticity decreases with increasing microjet pressure, and similar to the trend observed in figure 11, this reduction saturates at the same pressure. As before, there is an inverse correlation between the peak azimuthal vorticity and the reduction of the unsteady pressure loads. This once again suggests that the effectiveness of microjet control is also closely related to the redistribution of the azimuthal vorticity. By reducing azimuthal vorticity and increasing the shear layer thickness in the initial region of the jet flow, microjet control leads to a more stable impinging jet flow field.

(ii) *The streamwise vorticity field*

In earlier studies (Alvi *et al.* 2003; Lou *et al.* 2006), it was conjectured that the redirection of the azimuthal vorticity by microjets in the streamwise direction weakens the primary instabilities/structures in shear layer, thus providing effective control. This was partially based on the presence of streamwise streaks observed in the shadowgraphs and the presence of 'corrugated' structures in the cross-stream

visualizations of the jet shear layer using planar laser scattering (Lou *et al.* 2006). Prompted by this visual evidence, a quantitative examination of the role of microjets was conducted using stereoscopic PIV, where measurements at selected cross-planes of the jet flow field were obtained. Unless specified, the stereoscopic PIV results discussed here are for cases where 16 microjets are used; inclined at an angle of 60° and operated at 100 psia.

The cross-plane mean velocity fields, measured at three different axial locations ($x/d = 1.0$, 1.5, and 2.0) are shown in figure 17, capture the three-dimensional features of jet evolution. The data shown here were obtained by ensemble-averaging 400 instantaneous stereoscopic PIV whole-field measurements where the colour contours represent the streamwise, U_x, component of the velocity. In figure 17(*a*), the jet shear layer appears as a relatively smooth ring that becomes thicker due to the growth of the shear layer. However, with microjet control, figure 17(*b*), the shear layer displays a strongly modulated or 'corrugated' ring with a total of 16 indentations, where the azimuthal locations of these indentations correspond to the microjet positions around the nozzle periphery. These indentations become more diffused in the streamwise direction and eventually become difficult to individually identify at $x/d = 2$.

A closer examination of the velocity field with microjet control at the $x/d = 1$ cross-plane, shown in figure 18, reveals that relatively high radial velocities exist around these microjet-induced indentations. For the sake of clarity, only the distribution in the upper-left quadrant of the jet is shown here, where the in-plane velocity vectors are superimposed on the colour contours of the out-of-plane, i.e. streamwise, component. The vectors show that the core jet flow expands outward along the structure 'lobes' or peaks while ambient flow is entrained inward in the troughs. This substantial flow exchange between the ambient environment and the jet enhances the local mixing rate in the shear layer, increasing the shear layer thickness, a behaviour consistent with the measurements shown in figure 10. These cross-stream measurements also clearly reveal the flow three-dimensionality introduced due to the microjet-induced streamwise vortices.

In figure 19, we examine the ensemble-averaged streamwise vorticity distributions at the same cross-planes as in figure 17. A comparison of the no-control case, figure 19(*a*), to the microjet control data, figure 19(*b*), clearly shows that the activation of microjets introduces a higher level of coherent streamwise vorticity in the jet shear layer. Similar to the behaviour observed in figure 17(*b*), the spatially coherent vortical structures become more diffused in the downstream direction. However, compared to the baseline case of figure 19(*a*), the streamwise vorticity is still higher and more organized at downstream locations.

A more direct measure of the streamwise vorticity with and without control is seen in figure 20, which shows the vorticity distribution as a function of the azimuthal angle, at two locations, $x/d = 1$ and 2. In this figure, filled symbols correspond to the control case and the streamwise vorticity is measured at radial positions corresponding to the centre of the shear layer of the impinging jet. Again, taking advantage of the axisymmetric nature of the mean flow, the vorticity distribution is only shown for one quadrant of the jet periphery. Each counter-rotating vortex pair, induced by the microjets, can be identified here as an adjacent pair of a large-amplitude, vorticity peak/maximum (counter-clockwise vorticity) followed by a valley/minimum (clockwise vorticity). As expected, a total of four vorticity max–min pairs are clearly observed in one quadrant, where their locations roughly correspond to the points at which the microjets interact with the jet shear layer. In contrast,

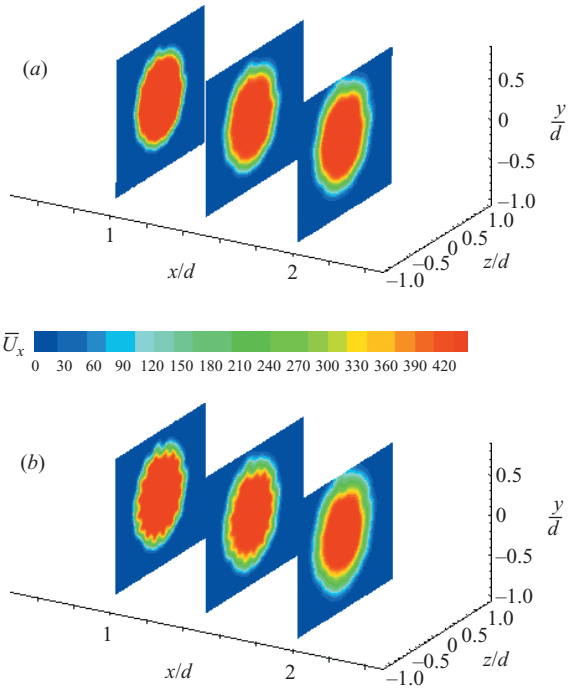

FIGURE 17. Mean axial velocity distribution at several streamwise locations; NPR = 3.7, $h/d = 4$. (*a*) No control, (*b*) with control.

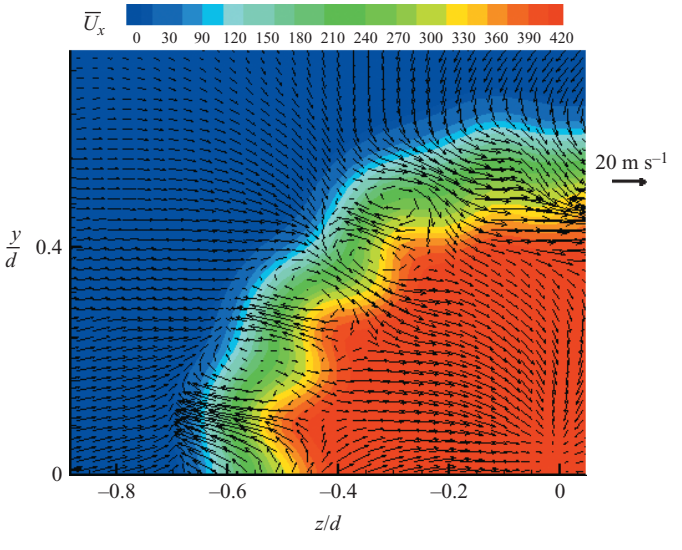

FIGURE 18. Details of the velocity field in the cross-plane at $x/d = 1$. NPR = 3.7, $h/d = 4$.

the vorticity for the uncontrolled jet is significantly lower and is not well-organized. At $x/d = 1$, the maximum normalized peak steamwise vorticity value with control is of the order of 1 (figure 20) and is substantial (about 25%) when compared to the maximum azimuthal shear layer vorticity without control, which is of the order of 4 (see figure 15). These results suggest that this substantial redirection of azimuthal vorticity into the streamwise direction plays a fundamental role in weakening the

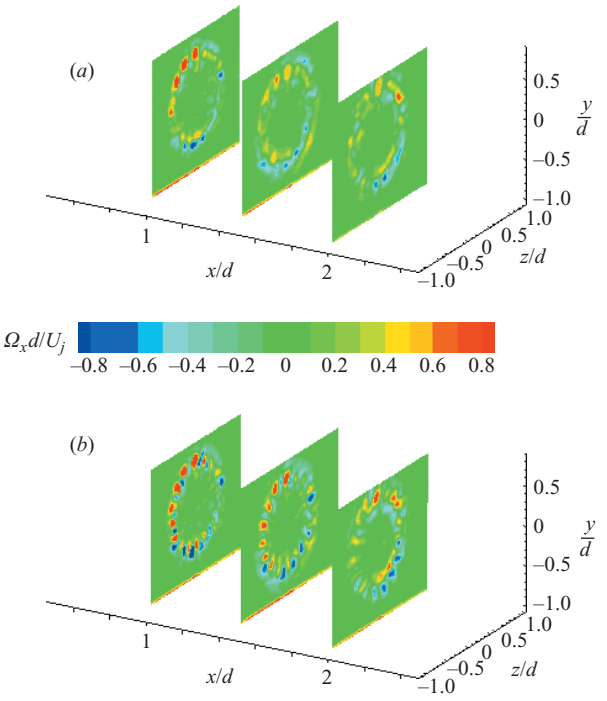

FIGURE 19. Ensemble averaged streamwise vorticity distribution in the cross-plane of the jet flow. NPR = 3.7, $h/d = 4$.

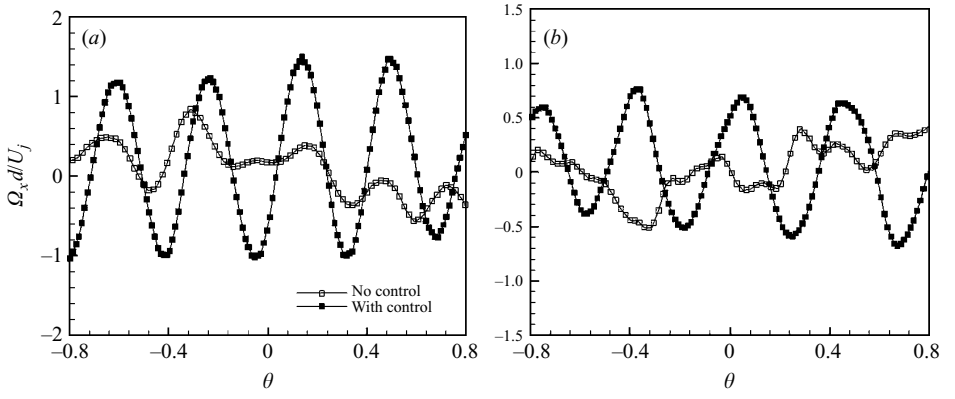

FIGURE 20. Ensemble-averaged streamwise vorticity distribution along the azimuthal direction, NPR = 3.7, $h/d = 4$. (*a*) $x/d = 1$; (*b*) $x/d = 2$.

primary flow stability and the subsequent reduction of the overall flow unsteadiness. Although the streamwise vorticity declines somewhat further downstream as seen in figures 19(*b*) and 20(*b*), it remains spatially coherent and at a much higher magnitude relative to the baseline case.

Finally, as briefly discussed in § 3.1.3, spacing appears to play a role in the efficacy of the microjet control scheme. In the present study, an inter-microjet spacing corresponding to a total of 16 microjets seems to be most efficient, within the confines of the present geometry and test conditions. This is supported by figure 21,

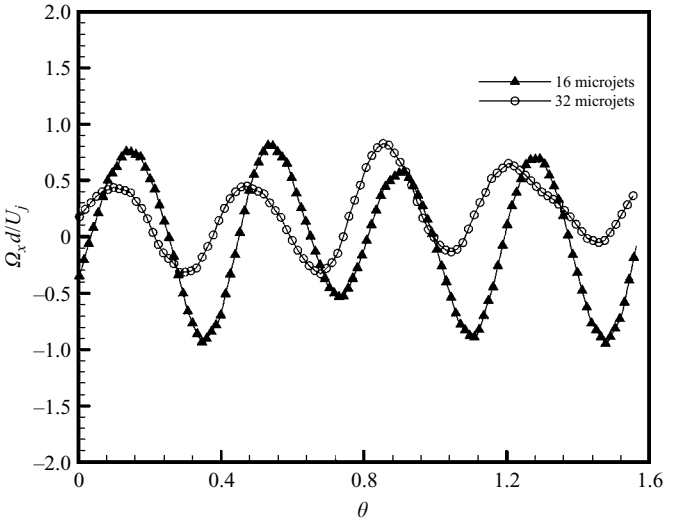

FIGURE 21. Effect of microjet spacing on the streamwise vorticity. NPR = 3.7, $h/d = 4$, $x/d = 1$, 60° microjet.

which shows a comparison of the azimuthal distribution of streamwise vorticity at a cross-plane of $x/d = 1$ using 16 and 32 microjets. As expected, four pairs of peak–valley distributions can be clearly identified in one quadrant, when 16 microjets are used. However, surprisingly, only four, instead of eight, peak–valley pairs are also observed when 32 microjets are used. This suggests that the streamwise vortices due to 32 microjets go through a pairing or merging process, upstream of this location. Unfortunately, $x/d = 1$ is the most upstream location for these cross-sectional PIV measurements and no direct evidence of vortex pairing or merging is available. The concept of vortex pairing and merging has been discussed by Zaman, Reeder & Samimy (1994) in their flow visualization study of vortices generated using delta tabs on jet flows. Before proceeding to a more detailed discussion of the vorticity field, we note that microjet injection was also discussed by Arakeri *et al.* (2003) who explored their use for transonic, $M = 0.9$, jet noise suppression. Although they did not present vorticity measurements, they suggested that the streamwise vorticity so generated is expected to be weak relative to the azimuthal vortex structures – in contrast to the evidence presented herein. In a very recent study, Alkislar, Krothapalli & Butler (2007) present elegant measurements of the streamwise vorticity introduced in a Mach 0.9 free jet through the use of chevrons (or tabs) and microjets. Their results, which focused on the effect of vorticity on the far-field aeroacoustics, clearly show the presence of streamwise vorticity due to both tabs and microjets.

3.3. *Further discussion: possible physical mechanisms*

Having shown that the microjets introduce substantial streamwise vorticity which affects the development of the primary jet, in this section we attempt to further examine the physical mechanisms behind microjet control. We note that what follows is not a rigorous analysis as it contains many assumptions and certain terms, such as those related to turbulent stresses, are not considered, in part because many of these terms are small and in part because many of these quantities have not been measured in this study. However, we believe that even such a simplified analysis, supported by direct measurements, provides some insight into the flow dynamics. In

this attempt to understand the origin of the vortical structures and determine the source of streamwise vorticity, the mean vorticity transport equation, is considered below:

$$\frac{\mathrm{D}\boldsymbol{\Omega}}{\mathrm{D}t} = \boldsymbol{\Omega}\cdot\nabla\boldsymbol{U} - \nabla\frac{1}{\rho}\times\nabla p + \upsilon\nabla^2\boldsymbol{\Omega} \tag{1}$$

where Ω, U, ρ, p represent the mean vorticity, mean velocity, density and pressure, respectively. This equation shows that the vorticity field can be convected, stretched, distorted and diffused. The second term on the right-hand side, which represents the baroclinic torque generation term, usually emerges when the pressure and density gradients are not aligned; this can be a significant source of vorticity generation in very high-speed flows (Marble, Zukoski & Jacobs 1990; Waitz, Marble & Zukoski 1992). However, as noted by Kim & Samimy (1999), the effect of streamwise vorticity generated by the baroclinic torque in an axisymmetric flow is usually negligible. In their study of turbulence-driven secondary motion in non-circular ducts, Demuren & Rodi (1984) examine the magnitude of velocity and Reynolds stress terms in the time-averaged vorticity equation for the streamwise component. They recommend accurate modelling of turbulent normal and shear stress terms as the magnitude of these terms is large although their signs are opposite. Liepmann & Gharib (1992) use their flow visualization and DPIV measurements to conclude that the streamwise vortices play an important role in the near-field entrainment and growth of the jet.

Although equation (1) does not contain other explicit source terms, new circulation can enter the flow through imposed initial conditions and/or boundary conditions. In the present study, one potential source of streamwise vorticity is the vorticity contained in the microjet streams. Based on an order-of-magnitude analysis, it can be easily shown that the collective circulation from all microjets is less than 10% of the circulation of streamwise vorticity measured in the primary jet when the microjets are activated. This suggests that a significant portion of the streamwise vorticity must come from existing vorticity through other processes, in particular the stretching or tilting of the azimuthal vorticity since this is the strongest component of vorticity in the present flow as seen in the visualizations and the flow-field measurements presented earlier.

To illustrate this further, the transport of the streamwise vorticity component (Ω_x) can be described using the following equation, if both the baroclinic and the diffusion terms are neglected:

$$\frac{\mathrm{D}\Omega_x}{\mathrm{D}t} = \Omega_x\frac{\partial U_x}{\partial x} + \Omega_\theta\frac{1}{r}\frac{\partial U_x}{\partial\theta} + \Omega_r\frac{\partial U_x}{\partial r}. \tag{2}$$

Here the first term on the right-hand side represents a stretching of the existing streamwise vorticity under an axial or streamwise velocity gradient, i.e. $\partial U_x/\partial x$. This term is important if the flow is accelerating locally as is the case for flow in the vicinity of the nozzle exit of an under-expanded jet. This is in part why, all else being equal, microjets are consistently more effective in controlling under-expanded jets. The second and third terms represent the tilting of the azimuthal (Ω_θ) and radial (Ω_r) vorticity, respectively, into the streamwise direction. For an axisymmetric jet without control, these two terms are usually negligible. Therefore, in order to redistribute these two components of vorticity into the streamwise direction, microjet control must introduce a higher velocity gradient along the azimuthal direction, $\partial U_x/r\partial\theta$, and/or generate significant radial vorticity, Ω_r (since there is already a strong velocity gradient across the shear layer, $\partial U_x/\partial r$).

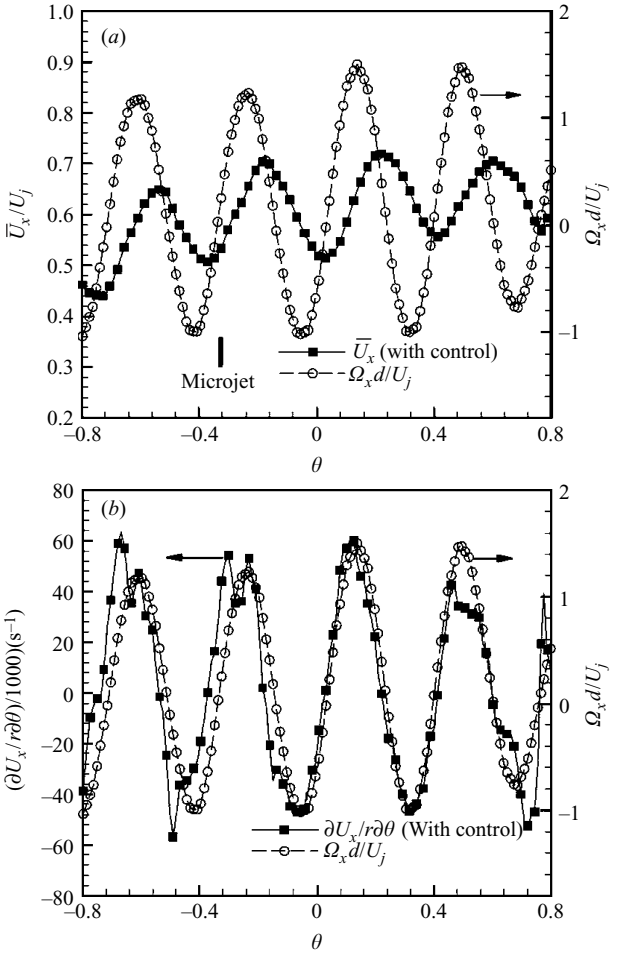

FIGURE 22. (*a*) Mean axial velocity and streamwise vorticity distribution along the azimuthal direction, and (*b*) correlation between $\partial U_x/r\partial\theta$ and $\Omega_x d/U_j$, at cross-plane of $x/d = 1$, $r/d = 0.55$, NPR = 3.7, $h/d = 4$.

Figure 22(*a*) shows the azimuthal distributions of the mean axial velocity, $\overline{U}_x$, and the normalized streamwise vorticity, $\Omega_x d/U_j$, at a radius of $r/d = 0.55$. For an axisymmetric jet without control, the mean axial velocity along the azimuthal direction is by definition constant. However, microjet control significantly changes the mean axial velocity distribution, as seen in figure 22(*a*). A distinct wavy pattern consisting of four modulations is seen in this plot when the microjets are on. It should be noted that this pattern is not a transient phenomenon since it persists in the ensemble average of 400 instantaneous PIV realizations used for this plot.

The corresponding azimuthal location of a representative microjet is marked by the thick vertical line near the lower axis of the graph where the microjet is roughly located at the minimum of the mean axial velocity distribution. This suggests that the presence of microjet streams locally decelerates the main jet flow, an observation consistent with the flow behaviour expected of a (micro)jet in a cross-flow. These local minima and maxima result in a higher azimuthal gradient of the mean axial velocity, $\partial U_x/\partial\theta$, along the azimuthal direction for the control case.

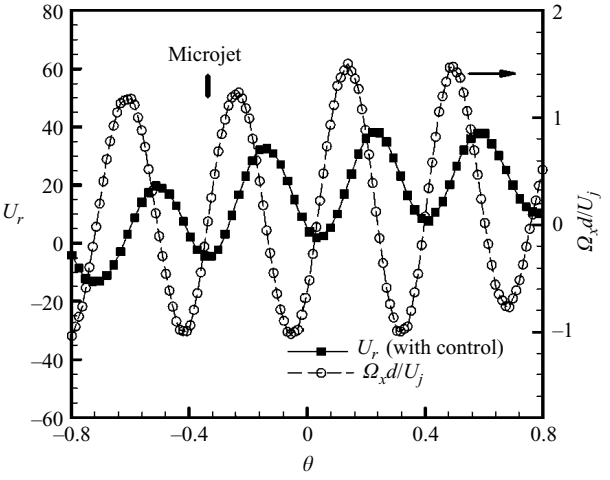

FIGURE 23. Mean radial velocity and streamwise vorticity distribution along the azimuthal direction at cross-palne, $x/d = 1$, $r/d = 0.55$, NPR $= 3.7$, $h/d = 4$.

Although we did not measure this term closer to the nozzle exit where microjets first interact with the primary jet shear layer, we believe this strong gradient term must exist further upstream (of $x/d = 1$) due to the blockage effect from the microjet streams. Since this gradient is multiplied by the strong azimuthal vorticity, Ω_θ, in the second term on the right-hand side of equation (2), it contributes to the redirection of the azimuthal vorticity into the streamwise direction, resulting in an increase of the rate of streamwise vorticity generation, $\mathrm{D}\Omega_x/\mathrm{D}t$, closer to the nozzle. This upstream generation through vorticity redistribution will undoubtedly lead to the increase of streamwise vorticity, Ω_x, further downstream as seen in the measurements at $x/d = 1$. A comparison of the open and filled symbols in figure 22(a) shows a clear correlation between the azimuthal velocity gradient of the axial velocity, $\partial U_x/\partial\theta$, and the presence of the streamwise vorticity for the microjets control case. To further illustrate this, in figure 22(b) we plot distributions of the azimuthal gradient of the streamwise velocity, $\partial U_x/r\partial\theta$, and the normalized streamwise vorticity. The remarkable match between the locations of the local minima and maxima of these terms provides strong circumstantial evidence regarding the role played by the mean axial velocity gradient, $\partial U_x/r\partial\theta$ in generating streamwise vorticity.

Next, we consider the contribution from the third term, $\Omega_r(\partial U_x/\partial r)$, in the streamwise vorticity transportation equation (2). Although there is a strong axial velocity gradient, $\partial U_x/\partial r$, across the jet shear layer, the shear layer of the uncontrolled axisymmetric jet does not have a substantial radial vorticity component, Ω_r. Hence, the radial vorticity, if present, must come from other sources. This is explored by examining the vorticity equation along the radial direction, written as

$$\frac{\mathrm{D}\Omega_r}{\mathrm{D}t} = \Omega_x\frac{\partial U_r}{\partial x} + \Omega_r\frac{\partial U_r}{\partial r} + \Omega_\theta\frac{1}{r}\frac{\partial U_r}{\partial\theta}. \tag{3}$$

This equation characterizes the source terms in the generation and/or redistribution of the radial vorticity. In particular, the third term on the right-hand side, $\Omega_\theta(1/r)(\partial U_r/\partial\theta)$, the tilting of the azimuthal vorticity component, generates radial vorticity. Figure 23 shows the azimuthal distribution of the mean radial velocity, U_r, and the streamwise vorticity at a radius of $r/d = 0.55$ with microjet control. The

blowing of a microjet (especially that placed at a high jet injection angle, 60° or 90°) can produce strong radial streams which cause the azimuthal vorticity to 'bend' in the radial direction. As a result, a significant amount of the radial vorticity component can potentially be generated by the redirection of the azimuthal component. This radial vorticity in turn can be tilted into the streamwise direction by the presence of a steep velocity gradient, $\partial U_x/\partial r$, in the jet shear layer, the third term on the right-hand side in equation (2).

Intuitively, this mechanism appears to be less effective since it requires the additional step of generating the radial vorticity component from the azimuthal vorticity. However, the velocity gradient across the shear layer, $\partial U_x/\partial r$ is an order of magnitude higher than the gradient along the azimuthal direction, $\partial U_x/r\partial\theta$. In the light of this discussion, the effect of the microjet injection angle on streamwise vorticity generation displays two opposing trends. On one hand, the contribution of the second term on the right-hand side in equation (2) to streamwise vorticity generation is expected to increase when the microjet injection angle is reduced, because microjets that are more in the direction of the primary jet will lead to larger $\partial U_x/\partial\theta$. This suggests that the 20° microjets should be more effective. In contrast, the contribution of the third term on the right-hand side would be enhanced for higher microjet angles, as this would result in a larger $\partial U_r/\partial\theta$ hence a higher Ω_r in equation (3). This in turn increases the contribution of the third term on the right-hand side of equation (2), suggesting that 90° microjets should be more effective from this perspective. This phenomenological argument is supported by our results, where we find that for most cases the 60° injection angle, a compromise between the two limits, is most efficient in terms of control. Through a better understanding of the physical mechanisms that lead to enhanced generation and growth of streamwise vorticity, one may be able to design control systems that maximize the combined contribution of both terms.

4. Summary

In this paper, the results of an experimental investigation of the flow and acoustic properties of a supersonic impinging jet, with and without control, are described. The near-field acoustic measurements clearly show that microjet control can either eliminate or significantly suppress the impinging tones. In addition, perhaps more significantly, the attenuation in the discrete tones is accompanied by a broad-band noise reduction indicating an overall decline of the unsteadiness in the jet flow with control. The near-field OASPL is reduced by up to 8 dB and the reduction in the unsteady pressure loads by up to 12 dB. The effects of some important control parameters including microjet angle, microjet pressure and microjet spacing are discussed in this paper.

The PIV measurements reveal that the activation of the microjets introduces strong and well-organized streamwise vorticity in the jet shear layer. This increase is concomitant with a decrease in the azimuthal vorticity. The velocity field measurements in the jet streamwise central plane clearly show that azimuthal vorticity is significantly reduced when the microjets are activated where the peak value of the azimuthal vorticity can be reduced by as much as 40% at NPR = 5. The combined effect of an increase in the shear layer thickness and a decrease of the peak azimuthal vorticity efficiently suppresses the primary shear layer instability, thus weakening the large-scale structures and upstream-propagating acoustic waves that are generated upon their impingement on the ground. This reduction of azimuthal

vorticity is believed to be the direct result of vorticity being redirected into the streamwise direction through tilting and stretching processes. Detailed 3-component PIV measurements in the jet cross-planes reveal a clear correlation between the azimuthal gradient of mean axial and radial velocity and the presence of the streamwise vorticity for the microjet control case, further confirming the role of the former in generating the latter. The emergence of three-dimensionality due to the streamwise vorticity further disrupts the spatial coherence of the coupling between the acoustic wave and shear layer instability. This sequence of events leads to the weakening of the feedback loop, and the subsequent reduction of the overall unsteadiness of the supersonic impinging jet flow.

This work was supported by a grant from AFOSR, monitored by Dr J. Schmisseur. We are grateful for their support. We would like to thank the staff of AAPL, for their invaluable help in conducting these tests. We are grateful for the assistance provided by Dr Alkislar in making the PIV measurements and Dr Choutapalli for his help in conducting the tests.

REFERENCES

Alkislar, M. B., Krothapalli, A. & Butler, G. W. 2007 The effect of streamwise vortices on the aeroacoustics of a Mach 0.9 jet. *J. Fluid Mech.* **578**, 139–169.

Alvi, F. S. & Iyer, K. 1999 Mean and unsteady properties of supersonic impinging jets with lift plates. *AIAA Paper* 99–1829.

Alvi, F. S., Shih, C. Elavarasan, R., Garg, G. & Krothapalli, K. 2003 Control of supersonic impinging jet flows using supersonic microjets. *AIAA J.* **41**, 1347–1355.

Arakeri, V. H, Krothapalli, A., Siddavaram, V., Alkislar, M. B. & Lourenco, L. M. 2003 On the use of microjets to suppress turbulence in the Mach 0.9 axisymmetric jet. *J. Fluid Mech.* **490**, 75–98.

Bradshaw, P. 1987 Turbulent secondary flows. *Annu. Rev. Fluid Mech.* **19**, 53–74.

Carling, J. C. & Hunt, B. L. 1974 The near wall jet of a normally impinging, uniform, axisymmetric, supersonic jet. *J. Fluid Mech.* **66**, 159–176.

Demuren, A. O. & Rodi, W. 1984 Calculation of turbulence-driven secondary motion in non-circular ducts. *J. Fluid Mech.* **140**, 189–222.

Donaldson, C. DuP. & Snedeker, R. S. 1971*a* A study of free jet impingement. Part 1. Mean properties of free and impinging jets. *J. Fluid Mech.* **45**, 281–319.

Donaldson, C. DuP. & Snedeker, R. S. 1971*b* A study of free jet impingement. Part 2. Free jet turbulent structure and impingement heat transfer. *J. Fluid Mech.* **45**, 477–512.

Elavarasan, R., Krothapalli, A., Venkatakrishnan, L. & Lourenco, L. 2000 A PIV study of a supersonic impinging jet. *J. Visualization* **2**, 213–222.

Greska, B. 2005 Supersonic jet noise and its reduction using microjet injection. Dissertation, Florida State University, Tallahassee.

Henderson, B. 2002 The connection between sound production and jet structure of the supersonic impinging jet. *J. Acoust. Soc. Am.* **111**, 735–747.

Henderson, B., Bridges, J. & Wernet, M. 2005 An experimental study of the oscillatory flow structure of tone-producing supersonic impinging jets. *J. Fluid Mech.* **542**, 115–137.

Julien, S., Lasheras, J. & Chomaz, J.-M. 2003 Three-dimensional instability and vorticity patterns in the wake of a flat plate. *J. Fluid Mech.* **479**, 155–189.

Kalghatgi, G. T. & Hunt, B. L. 1976 The occurrence of stagnation bubbles in supersonic jet impingement flows. *Aero. Q.* **27**, 169–185.

Karamcheti, K., Bauer, A. B., Shields, W. L., Stegen, G. R. & Woolley, J. P. 1969 Some features of an edge tone flow field. *NASA SP* **207**, 275–304.

Kegerise, M. A., Spina, E. F., Garg, S. & Cattafesta, L. N. 2004 Mode-switching and nonlinear effects in compressible flow over a cavity. *Phys. Fluids.* **16**, 678–687.

Kim, J. H. & Samimy, M. 1999 Mixing enhancement via nozzle trailing edge modifications in a high speed rectangular jet. *Phys. Fluids.* **11**, 2731–2742.

Krothapalli, A., Rajakuperan, E., Alvi, F. S. & Lourenco, L. 1999 Flow field and noise characteristics of a supersonic impinging jet. *J. Fluid Mech.* **392**, 155–181.

Lasheras, J. C. & Meiburg, E. 1990 Three-dimensional vorticity modes in the wake of a flat plate. *Phys. Fluids* A. **2**, 371–380.

Liepmann, D. & Gharib, M. 1992 The role of streamwise vorticity in the near-field entrainment of round jets. *J. Fluid Mech.* **245**, 643–668.

Lou, H. 2005 Control of supersonic impinging jets using microjets. Dissertation, Florida State University, Tallahassee.

Lou, H., Alvi, F. S. & Shih, C. 2006 Active and passive control of supersonic impinging jets. *AIAA J.* **44**, 58–66.

Lourenco, L. & Krothapalli, A. 1998 Mesh-free, second order accurate algorithm for PIV processing. *Proc. Intl Conf. on Optical Technology and Image Processing in Fluid, Thermal and Combustion Flow, Yokohama, Japan*, p. 224.

Marble, F. E., Zukoski, E. E. & Jacobs, J. W. 1990 Shock enhancement and control of hypersonic mixing and combustion. *AIAA Paper* 1990–1981.

Meiburg, E. & Lasheras, J. C. 1988 Experimental and numerical investigation of the three dimensional transition in plane wakes. *J. Fluid Mech.* **190**, 1–37.

Neuwerth, G. 1974 Acoustic feedback of a subsonic and supersonic free jet which impinges on an obstacle. *NASA TT F*-15719.

Papamoschou, D. & Hubbard, D. 1993 Visual observation of supersonic transverse jets. *Exps. Fluids* **14**, 468–476.

Pierrehumbert, R. T. & Widnall, S. E. 1982 The two- and three-dimensional instabilities of a spatially periodic shear layer. *J. Fluid Mech.* **114**, 59–82.

Powell, A. 1988 The sound-producing oscillations of round under-expanded jets impinging on normal plates. *J. Acoust. Soc. Am.* **83**, 515–533.

Samimy, M., Zaman, K. B. M. Q. & Reeder, M. F. 1993 Effect of tabs on the flow and noise field of an axisymmetric jets. *AIAA J.* **31**, 609–619.

Sheplak, M. & Spina, E. F. 1994 Control of high-speed impinging-jet resonance. *AIAA J.* **32**, 1583–1588.

Shih, C., Alvi, F. S. & Washington, D. 1999 Effects of counterflow on the aeroacoustic properties of a supersonic jet. *J. Aircraft* **36**, 451–457.

Tam, C. K. W. 1988 The shock-cell structures and screech tone frequencies of rectangular and non-axisymmetric supersonic jets. *J. Sound Vib.* **121**, 135–147.

Tam, C. K. W. & Ahuja, K. K. 1990 Theoretical model of discrete tone generation by impinging jets. *J. Fluid Mech.* **214**, 67–87.

Waitz, I. A., Marble, F. E. & Zukoski, E. E. 1992 Vorticity generation by contoured wall injectors. *AIAA Paper* 92-3550.

Widnall, S. E., Bliss, D. B. & Tsai, C. -Y. 1974 The instability of short waves on a vortex ring. *J. Fluid Mech.* **66**, 35–47.

Zaman, K. B. M. Q. 1999 Spreading characteristics of compressible jets from nozzles of various geometries. *J. Fluid Mech.* **383**, 197–228.

Zaman, K. B. M. Q., Reeder, M. F. & Samimy, M. 1994 Control of an axisymmetric jet using vortex generators. *Phys. Fluids.* **6**, 778–793.